STRUCTURE OF EDGE-PLASMA TURBULENCE IN THE CALTECH TOKAMAK*

S.J. ZWEBEN**, R.W. GOULD
California Institute of Technology,
Pasadena, California,
United States of America

ABSTRACT. Measurements of the spatial structure of tokamak edge density fluctuations $\tilde{n}$ have been made using compact probe arrays in the Caltech tokamak. The results indicate that the structure of $\tilde{n}$ in the tokamak edge is characterized by very short auto-correlation times and short cross-correlation lengths, i.e. that the edge density fluctuations consist of small-scale 'turbulence'. The space-time structure of this $\tilde{n}$ turbulence is consistent with several recent non-linear edge instability models. The structure of the local electrostatic potential $\tilde{\phi}$ is measured to be qualitatively similar to that of $\tilde{n}$, and local cross-correlation between $\tilde{n}$ and $\tilde{\phi}$ indicates large outward radial particle transport similar to predictions of the edge instability models.

1. INTRODUCTION

In this paper we describe detailed measurements of the space-versus-time structure of density and potential turbulence in the edge region of the Caltech tokamak. These results are an extension of the single-probe scaling measurements reported previously for this tokamak [1].

Information on the spatial structure of tokamak turbulence is of interest primarily because it provides a check of our understanding of the small-scale state of the plasma. In particular, these experimental results are at least qualitatively similar to those obtained from recent non-linear theoretical models which emphasize the strongly turbulent character of the edge plasma [2-6]. The improved connection between experiment and theory in this area should eventually lead to an understanding of the transport effects caused by this kind of turbulence [7, 8].

The paper is organized as follows: Section 2 contains the experimental details concerning the tokamak and the probe arrays; Section 3 presents the results from the 1-D poloidal array; in Section 4, results from the 2-D radial versus poloidal array are presented; Section 5 describes measurements of particle transport; Section 6 is a discussion, and Section 7 is a summary of the results.

2. EXPERIMENTAL DETAILS

The Caltech tokamak has been described previously in the context of single-probe edge turbulence scaling measurements [1]. The major and minor radii of the torus are R = 45 cm and a = 16 cm, and the toroidal field and plasma current are B_T = 3.5 kG and I = 20 kA, i.e. q (a) = 5. The central electron temperature is estimated from the conductivity to be $T_e(0) \approx 100$ eV at Z_{eff} = 2, and the line-averaged density is variable with gas puffing in the range $\bar{n} = 10^{12} - 10^{13}$ cm^{-3}. Although the central plasma parameters are different from those of larger tokamaks, the edge parameters of T_e = 5–25 eV and n = 3 × 10^{11} – 3 × 10^{12} cm^{-3} at r/a = 0.8–1.0 are quite similar to the edge parameters of most tokamaks [9]. All data in the present paper are taken during the steady-state phase of normal discharges in this tokamak, for which $T_e \cong$ 25 eV and n $\cong 10^{12}$ cm^{-3} at r/a = 0.8.

The probe arrays used for these measurements are depicted in Fig.1. The 1-D poloidal array consists of 32 Langmuir probes, each 0.1 cm in diameter, spaced 0.24 cm apart along a 7.5 cm arc at the outer equatorial plane. These probes extend radially 0.3 cm into the plasma and are mounted on a grounded stainless-steel support structure shaped to fit the curvature of the plasma (the probes are made of tungsten). The 2-D radial-versus-poloidal probe array consists of an 8 × 8 square matrix of Langmuir probes, each 0.16 cm in diameter, which are mounted on the ion-drift side of a grounded stainless-steel support structure located at the outer equatorial plane (the two probe arrays were not in the chamber at the same time). The probe
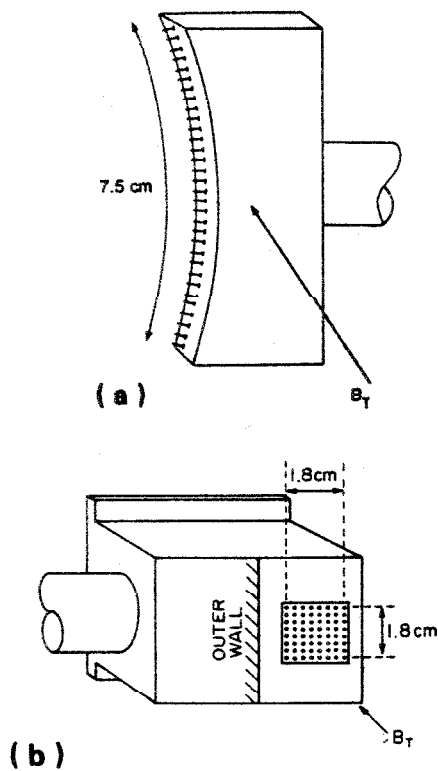
FIG.1. Probe construction for the (a) 32-probe 1-D and
(b) 64-probe 2-D arrays. Both probe arrays are inserted at the
outer equatorial plane of the tokamak. The 1-D array is radially
movable, but the 2-D array is fixed with respect to the outer
wall as shown.

array is necessarily blocked on one side by the probe
support structure, so that strictly speaking these
2-D turbulence patterns are obtained only in the
'scrape-off' layer or limiter shadow region of the probe
array itself. However, previous measurements have
shown that the turbulence is at least qualitatively
similar with or without the presence of a limiter [1];
also, the poloidal structure of $\tilde{n}$ as measured by the
shadowed 2-D array is very similar to the poloidal
structure measured by the unshadowed 1-D array, and
the 2-D $\tilde{n}$ structure is also unchanged when the probe
support structure is floated instead of grounded (and ·
the probes are biased with respect to the chamber).
Thus we can tentatively assume that these 2-D edge
turbulence results are approximately the same as
would be present without the intervening probe support
structure.

The data for the 1-D poloidal array were generally
recorded at a sampling rate of 400 kHz with an analog
bandwidth of $\gtrsim 200$ kHz. Data for the 2-D array were
recorded at a sampling rate of 1.6 MHz with an analog
bandwidth of $\gtrsim 200$ kHz using a specially built fast-
digitizing system [10]. This high sampling rate for the
2-D array was necessary in order to prepare a 2-D
space-versus-time film of these data (available on
request from the authors).

3. 1-D POLOIDAL DENSITY STRUCTURE

3.1. Poloidal correlation length

Typical data on the poloidal structure of the edge
density turbulence are shown in Fig.2. Figure 2(a)
shows raw data on the fluctuating parts of the
32 probe signals versus time, and in 2(b) is a greyscale
plot with higher-than-average n for each probe
represented as darker regions and lower-than-average n
represented as lighter regions. For this case, the probes
were placed 2.2 cm into the chamber ($r/a = 0.86$),
where $\tilde{n}/n = 47 \pm 5\%$ for all probes.

The basic nature of the 1-D poloidal structure can
be seen from the raw data. There is no predominant
periodic structure in space or time, and the spatial
correlations extend over only a fraction of the array
size. This is shown quantitatively in Fig.3(a) through
the cross-correlation functions $C_{1b}(\tau)$, where

$$C_{1b}(\tau) = \Sigma S_1(t)\, S_b(t+\tau) \Big/ \sqrt{(\Sigma S_1^2 \Sigma S_b^2)} \qquad (1)$$

and τ is the delay time between the two signals, S_1
refers to probe signal No.1, S_b refers to the other probe

spacing is 0.26 cm and each probe extends 0.6 cm into
the toroidal field direction. The total extent of the
probes in this array is 1.8 cm in both poloidal and
radial directions, which corresponds to a radial range
of $r/a = 0.85 - 0.95$. The probes in the 2-D array are
gold-coated and are mounted on a Macor insulating
square as shown.

For measurements of the $\tilde{n}$ spatial patterns, each
probe is biased separately to collect the ion saturation
current J^+ similarly to the single-probe measurements
described previously [1], i.e. the fluctuations in J^+ are
equated to the fluctuations in local density. For
measurements of potential fluctuations, these probes
are each operated to measure the floating potential ϕ_f
across 100 kΩ with respect to the grounded probe
support structure. Measurements of the electron
temperature and space potential are obtained from
swept-probe characteristics.

Although there are no localized limiters in this
tokamak, it is important to note that the 2-D probe

signals, and where the signals are summed over a time interval of T = 0.8 ms.

A measure of the poloidal correlation length L_p can be obtained from the zero-time cross-correlation coefficient $C_{1b}(0)$ versus probe separation, as is shown in Fig.3(b). Defining the correlation length as the distance over which the zero-time correlation falls from 1.0 (at b = 1) to 0.6, we find for these data L_p = 1.2 cm. Figure 3(c) shows correlation-versus-separation plots for several shots in which probe No.16 was cross-correlated with the other probes (instead of probe No.1) in order to see the fall-off in both directions. Poloidal correlation lengths are again in the range of L_p = 1.0—1.5 cm, which is very small when compared to the minor radius a = 16 cm.
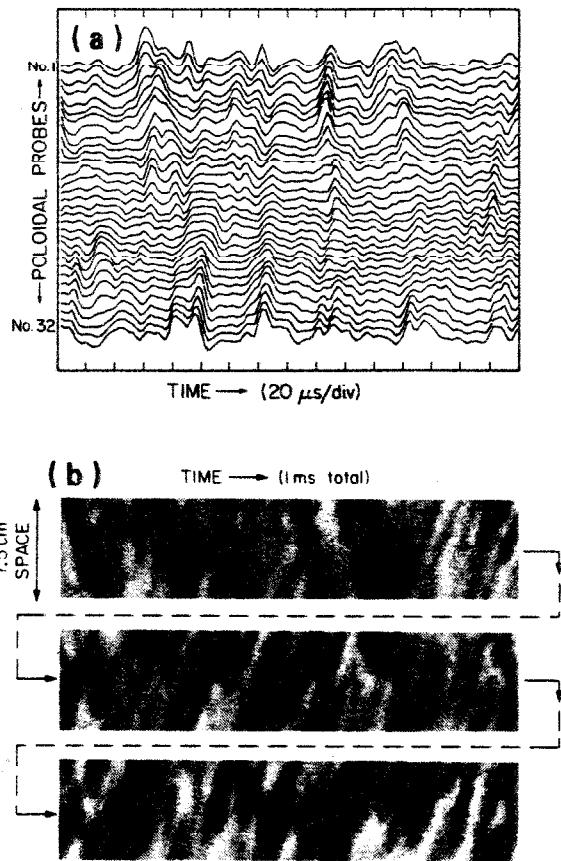

FIG.2. Data from the 32-probe 1-D poloidal array: (a) raw signals of $\tilde{n}$ versus time, (b) greyscale plot of $\tilde{n}$ versus time showing higher-than-average n for each probe as darker regions and lower-than average n as lighter regions (linear darkness scale). The data of part (a) correspond to the middle strip in part (b).
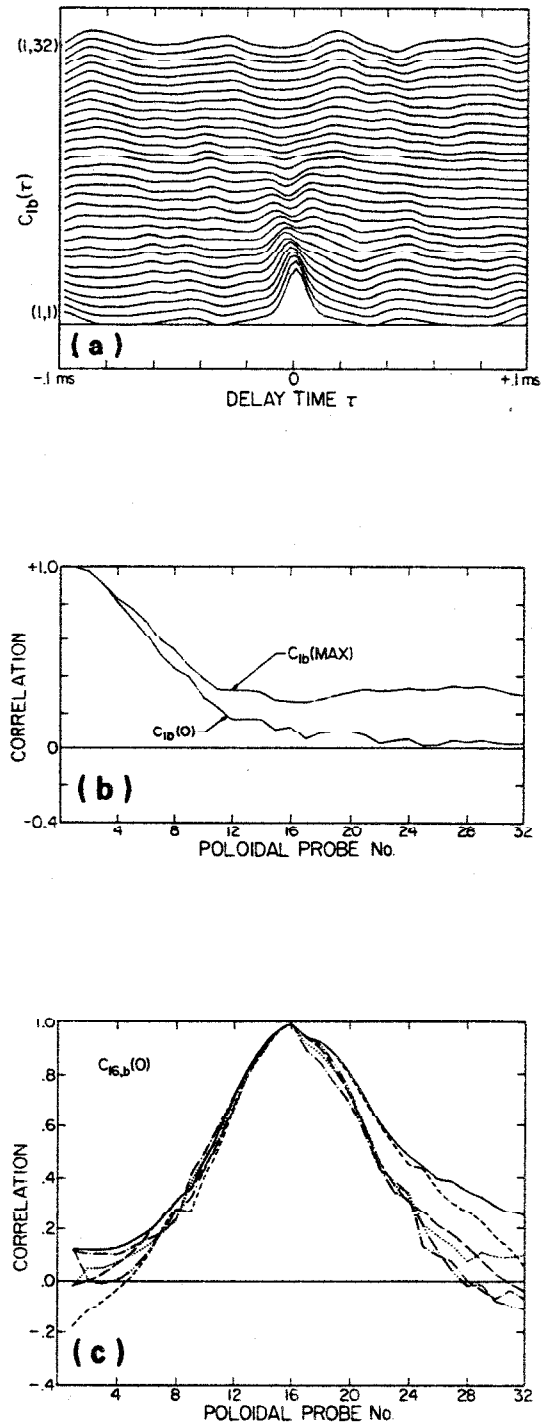
FIG.3. (a) Cross-correlation functions between probe 1 and the 32 probes in the 1-D poloidal array, with the auto-correlation function of probe 1 at bottom; (b) zero-time and maximum cross-correlation coefficients between probe 1 and the other probes in the 32-probe array; (c) cross-correlation functions between probe 16 and the 32 probes in the 1-D array for various shots. The averaging interval is T = 0.8 ms for these analyses, and the probe radial position is r/a = 0.86 for (a) and (b) and 0.86—0.90 for (c).
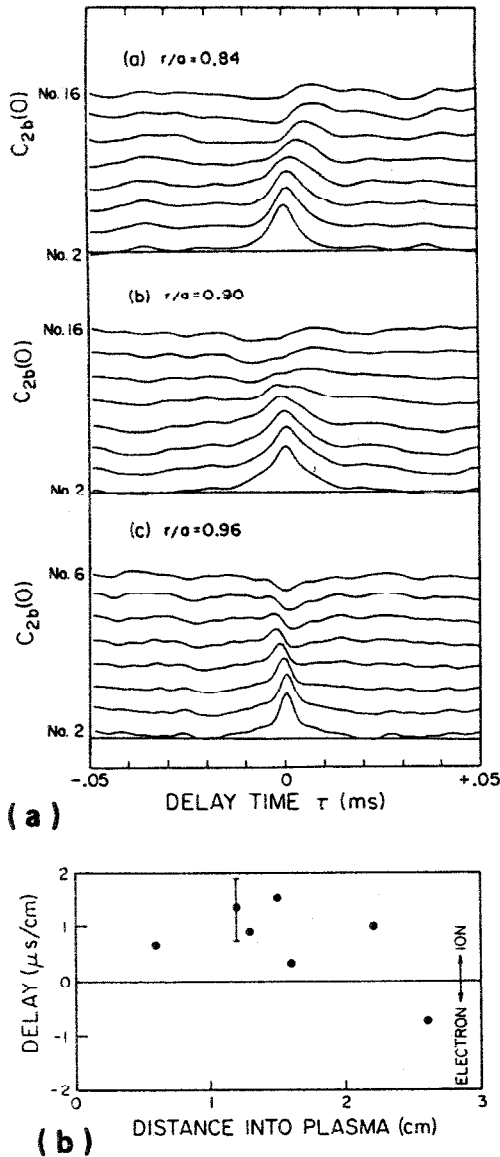
(a)

(b)

FIG.4. (a) Cross-correlation functions versus probe radius between probe No.2 and other probes in the 1-D array. Only even numbered probes are used here (the system bandwidth is also 400 kHz rather than the 200 kHz used for the 32-probe data). (b) poloidal propagation velocities versus radius of the probes, measured as the delay time to the peak of the cross-correlation function between probe No.2 and probe No.6 (poloidal separation 1.0 cm). Each point represents the average over several shots.

This propagation can be characterized by the delay time to the peak of the cross-correlation function measured between two nearby probes, as is shown in Fig.4(a). It is found that the propagation is predominantly in the ion diamagnetic direction near the wall, but reverses to the electron diamagnetic direction farther into the plasma, as is shown in Fig.4(b). A similar behaviour is seen in the 2-D array (Section 4.4). Note that even at a fixed radial position, the local direction and magnitude of the propagation velocity can vary in time, as can be seen by examining Fig.2(b).

This poloidal velocity does not propagate these disturbances very far in the poloidal direction before they are significantly distorted. This can be seen from the deterioration of the maximum value of the cross-correlation C_{1b} (MAX) (at any time) versus probe separation shown in Fig.3(b). Thus the 1-D turbulence pattern does not behave according to a 'frozen-flow' hypothesis, in part because the structure is actually 2-D (Section 4), such that local disturbances propagate radially as well as poloidally and so can disappear from the view of this 1-D array.
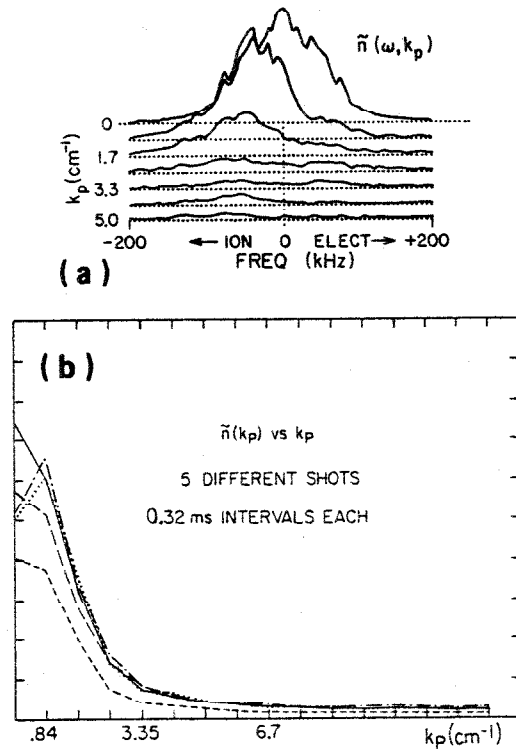

(a)

(b)

FIG.5. (a) Spectrum of $\tilde{n}$ (ω, k_p) for the 32-probe poloidal data at a probe position of $r/a = 0.96$. The frequency spectra are not corrected for the anti-aliasing filter (which reduces $\tilde{n}$ (ω) by X 0.6 at 100 kHz and X 0.1 at 200 kHz), (b) time-averaged $\tilde{n}$ (ω, k_p) spectra from several shots for the 32-probe 1-D data (r/a = 0.86-0.90). The spatial data were multiplied with a Hanning window before Fourier analysis.

3.2. Poloidal propagation

Another aspect of these data is the poloidal propagation of the $\tilde{n}$ fluctuations, which can be seen by the 'tilts' in the greyscale plot in Fig.2(b), and by the shift in time of the peak of the $C_{1b}(t)$ functions in Fig.3(a).

174

3.3. $\tilde{n}\,(\omega, k_p)$ spectrum

The 1-D data can be Fourier-analysed in space and time to give the local $\tilde{n}\,(\omega, k_p)$ spectrum, as shown in Fig.5(a). The frequency spectra are found to be broad at a fixed k_p, similar to the results of electromagnetic scattering experiments [7, 8]. In this case the peaks of the frequency spectra are shifted toward the left, which corresponds to a predominant phase velocity in the ion diamagnetic direction at this radius ($r/a = 0.96$).

The time-averaged k_p-spectra are shown in Fig.5(b). The peak of $\tilde{n}\,(k_p)$ occurs in the range $k_p = 0.5 \pm 0.5$ cm^{-1}, which at $k_p = 0.5$ cm^{-1} corresponds to a drift wave parameter of $k_p r_s \lesssim 0.1$, where r_s is the ion gyroradius evaluated at the electron temperature ($r_s \cong 0.15$ cm for the edge plasma in this experiment). This is approximately in the drift-wave turbulence range of wavenumbers (see Section 6.2).

4. RADIAL-VERSUS-POLOIDAL STRUCTURE

4.1. Radial profiles

The radial profiles of the average values of density and electron temperature across the 2-D array are shown in Fig.6(a). The temperatures were obtained as usual from the exponential part of slowly swept (≈ 1 ms) single-probe-current-versus-voltage characteristics. The density profile was obtained from the ion saturation current profile by assuming $J^+ \propto n\sqrt{T_e}$. The profile of the average space potential ϕ_s was also obtained from the knee of the same swept-probe characteristics used to evaluate T_e, and is approximately given by $\phi_s = +2.5-3.0\,T_e$ with respect to ground, while the average floating potential ϕ_f is flat to within about ± 10 volts of zero, as is shown in Fig.6(b). Similar profiles were obtained previously in this machine [11]. Note that the poloidal profiles are approximately constant across the array, because of the small poloidal angle covered ($7°$).

The radial profiles of the relative fluctuation levels $\tilde{n}/n$ and $e\tilde{\phi}_f/T_e$ over the full frequency range of $f = 10 - 1000$ kHz are shown in Fig.6(c). The fluctuation spectrum of $\tilde{n}$ and the radial profiles of $\tilde{n}/n$ are similar to those found previously [1]. The fluctuation level of $\tilde{\phi}_f$ is shown in Fig.6(b); the spectrum of $\tilde{\phi}_f$ is similar to the spectrum of $\tilde{n}$. The radial profile of $e\tilde{\phi}_f/T_e$ is inferred from the measured $\tilde{\phi}_f$ and a straight line fit through the measured T_e points.
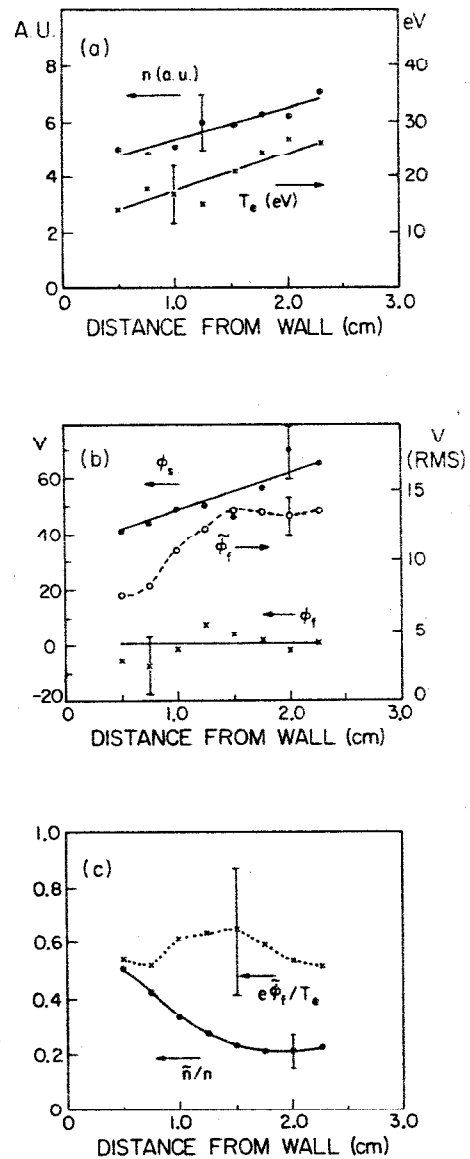

FIG.6. Radial profiles of various quantities as measured by the 2-D array: (a) average density and temperature profiles; (b) average space, ϕ_s, and floating, ϕ_f, potential profiles and $\tilde{\phi}_f$ profile; (c) relative fluctuation levels. The absolute density is approximately 10^{12} cm^{-3} at the innermost point.

An example of the time variation of the radial profile of J^+ is shown in Fig.7. The fluctuations are so strong that there are often short-lived local maxima in the radial profile.

Note that in the following Sections 4.2 to 4.4 the fluctuation properties were all measured with the 64 channel, 200 kHz data system rather than with the full 1 MHz bandwidth system used for Figs 6 and 7.
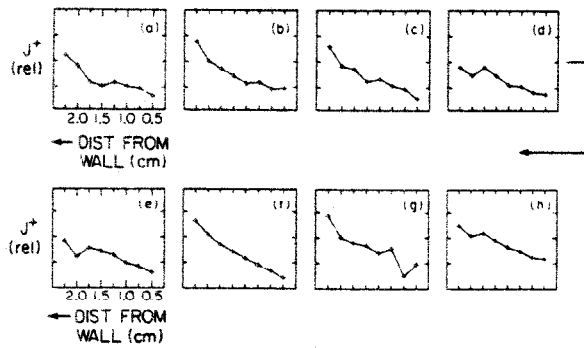
FIG.7. Instantaneous radial profiles versus time of J^+ for one radial row in the 2-D array. The sequence of profiles (a)–(h) are each separated by 2.5 µs (these data were taken with the full 1 MHz bandwidth system). The time-averaged density profile is shown in Fig.6(a).

Although the 200 kHz data system is sensitive to only about half of the total fluctuation amplitude, checks of the structural properties made with the full-bandwidth system showed that they were roughly the same as those measured using the lower-frequency system (e.g. the correlation lengths were about 40% smaller using the full-bandwidth system).

4.2. 2-D structure maps

Typical examples of the 2-D space-versus-time structure of the $\tilde{n}$ and $\tilde{\phi}_f$ turbulence are shown in Fig.8. These contour plots are made similarly to the greyscale plot of Fig.3(a), i.e. the higher-than-average values for each probe are shaded red, and the lower-than-average values are shaded blue. Although these plots therefore represent the *relative* density or potential fluctuation pattern, they also show approximately the absolute $\tilde{n}$ and $\tilde{\phi}_f$ patterns since the root-mean-square magnitudes of both $\tilde{n}$ and $\tilde{\phi}_f$ are also roughly constant across the array (Fig.6).

The 2-D structure of the potential turbulence is qualitatively similar to that of the density turbulence. In both cases the patterns can be loosely described as consisting of localized regions of relatively high- or low-density (or potential) which move irregularly both radially and poloidally through the area covered by the array. These localized 'blobs' can be tracked individually and their lifetimes and other properties can be studied statistically for evidence of possible organized structure within the turbulence [12]. However, in the remainder of this paper we discuss only the time-averaged properties of this turbulence.

4.3. Correlation lengths and k-spectra

A comparison of the radial-versus-poloidal correlations of $\tilde{n}$ is shown in Fig.9. In Fig.9(a), a probe from the top edge of the array is correlated with itself and the other seven probes in its poloidal row, and a probe from the outside edge of the array is correlated with itself and the other seven probes in its radial row. Evidently, the poloidal correlation length is longer than the radial correlation length for this case. This is shown more explicitly in Fig.9(b), where the zero-time correlations $C_{1b}(0)$ versus probe separation are shown for each of the eight poloidal and radial rows (for one shot).

The correlation lengths L_p and L_r can be obtained from plots of $C_{1b}(0)$ versus probe separation, as was discussed in Section 3.1. Figure 10 shows the resulting poloidal-versus-radial $\tilde{n}$ correlation lengths from several different data runs (each point represents the average over the eight poloidal or radial rows for one shot). Note that the L_r are actually the average of the radial correlation lengths measured separately from the two ends of the array (the L_r measured from the innermost probes are 40% smaller than those measured from the outermost probes). The poloidal correlation lengths (within this bandwidth) are $L_p = 1.1$ cm (i.e. roughly consistent with the 1-D array), while the radial correlation lengths are somewhat smaller, i.e. $L_r = 0.7$ cm.

The correlation lengths for the $\tilde{\phi}_f$ fluctuations were calculated similarly with results also shown in Fig.10. The asymmetry between radial and poloidal correlation lengths is somewhat more pronounced for the potential fluctuations, with $L_p = 1.2$ cm but $L_r = 0.5$ cm. Note that there was no significant radial variation of the poloidal correlation length, or poloidal variation of the radial correlation length, for either density or potential fluctuations across this array.

A typical two-dimensional $\tilde{n}(k_r, k_p)$ spectrum is shown in Fig.11. The broader radial spectrum corresponds to the shorter radial correlation length. Since the probes extend only 1.8 cm in either direction, the detailed structure below $k = 3.5$ cm^{-1} cannot be resolved as it was for the 7.5 cm poloidal array.

4.4. Propagation velocity

The poloidal propagation of the $\tilde{n}$ perturbations was calculated for each poloidal row from the delay time of the peak of the poloidal cross-correlation function (see Fig.9(a)). The results for $\tilde{n}$ shown in Fig.12 are similar to those found for the 1-D array (Fig.4); namely, the propagation switches from the
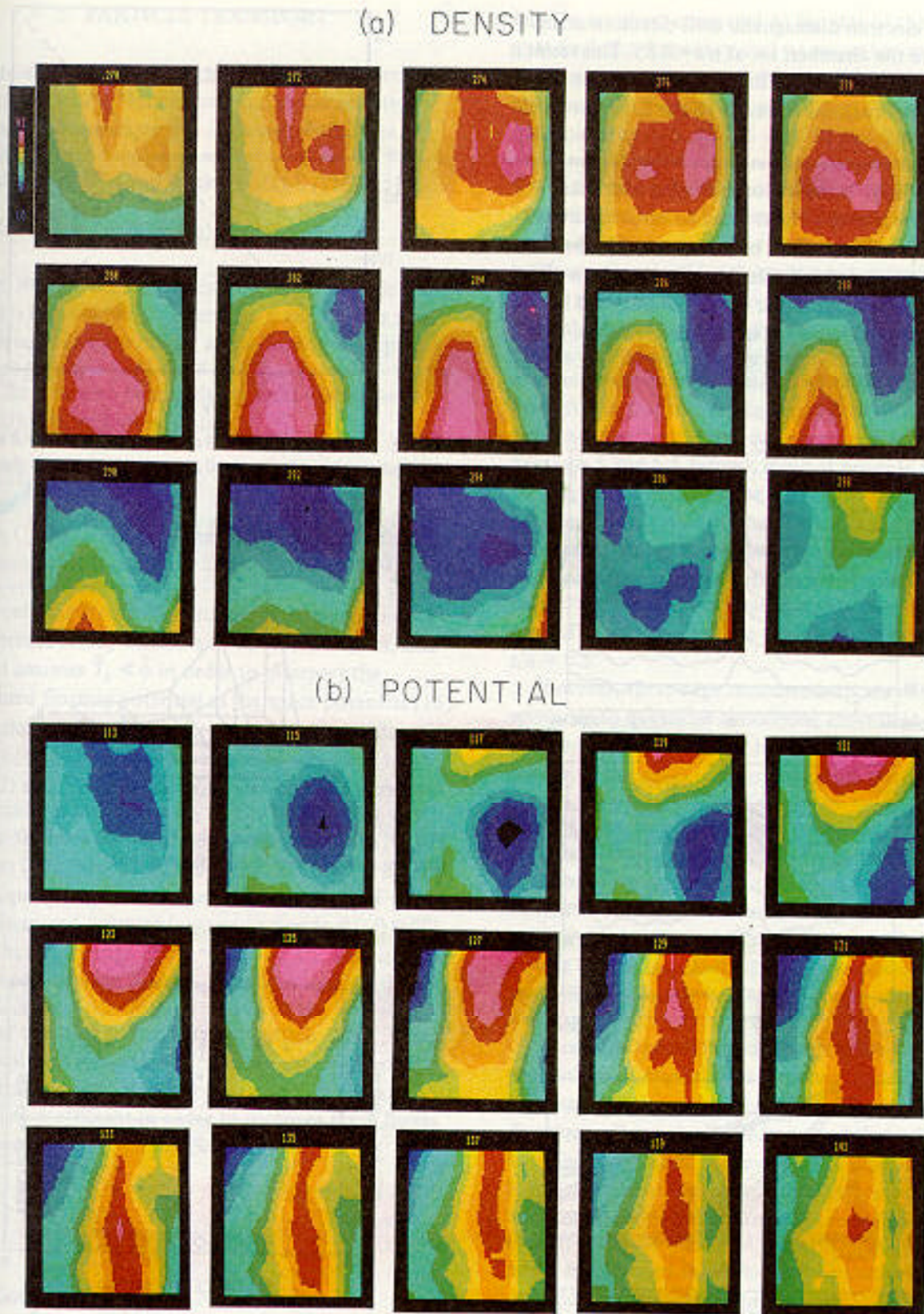
176

FIG.8. Contour plots of (a) ñ and (b) φ̄_f versus time as measured over the 2-D array. Fifteen frames are shown for both ñ and φ̄, with the time sequence starting from the upper left and proceeding to the lower right. The direction radially inward is toward the right in each frame, and the ion diamagnetic (poloidal) direction is downward in each frame. Higher-than-average n (or φ_f) for each probe are represented by red, and lower-than-average n (or φ_f) are represented by blue. Linear interpolation has been used between probes. The timescale is 1.2 μs between successive frames (a film is available from the authors).

ion to the electron diamagnetic drift direction at about 2.2 cm into the chamber, i.e. at r/a = 0.85. This result is discussed in Section 6.3. The poloidal propagation for the $\tilde{\phi}_f$ fluctuations is similar to the $\tilde{n}$, as shown in the figure.

The radial propagation velocities were also calculated in a similar way; however, on averaging over many shots there was only a slight trend towards an inward propagation velocity. This behaviour can also be seen in the trajectories of individual localized regions of $\tilde{n}$ [12], which can move either inward or outward but have a slight preference for inward propagation.

FIG.10. Poloidal versus radial correlation lengths for $\tilde{n}$ and $\tilde{\phi}_f$, averaged over time and over all the individual rows in the array.

FIG.11. Two-dimensional $\tilde{n}$ (k_r, k_p) for the 2-D array. These data are averaged over 0.3 ms for one shot.
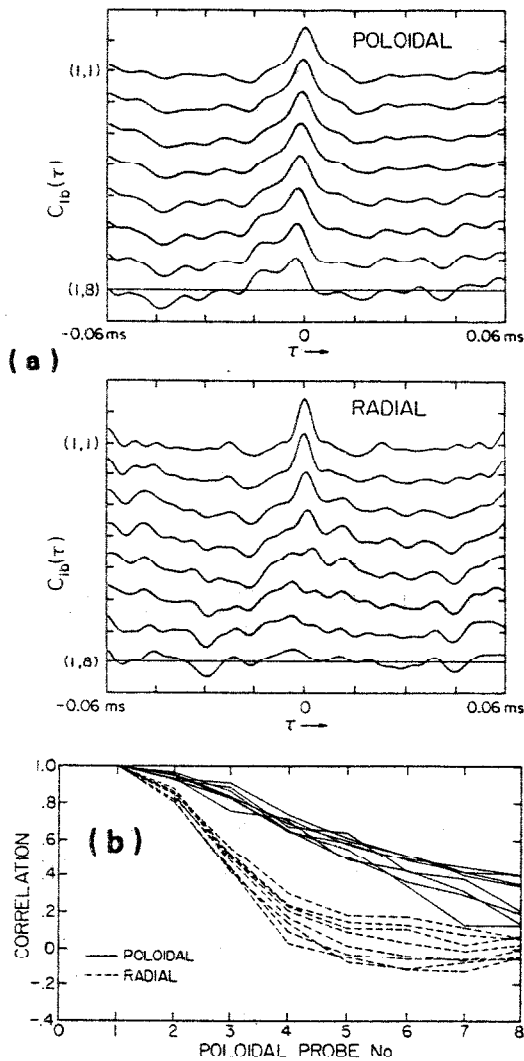

FIG.9. (a) Poloidal and radial cross-correlation functions of $\tilde{n}$ for two individual rows in the 2-D array; (b) poloidal and radial zero-time cross-correlation coefficients for each of the eight poloidal and eight radial rows for one shot. The averaging time interval was T = 0.3 ms for these analyses.
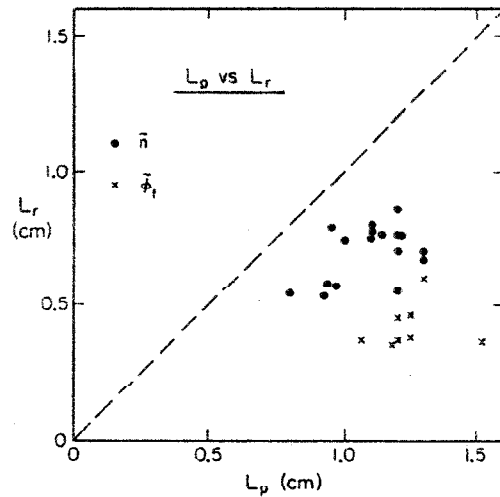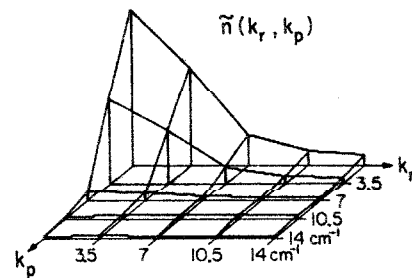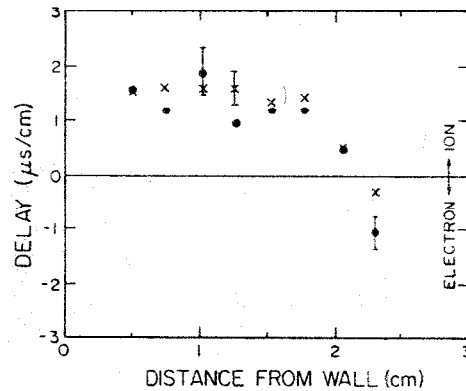

FIG.12. Poloidal propagation velocities of $\tilde{n}$ and $\tilde{\phi}_f$ versus radius for the eight poloidal rows of the 2-D array, measured as the delay time to the peak of the cross-correlation function between probes separated by 0.75 cm poloidally. Each point represents the average over several shots. Density points are labelled ●, while potential points are labelled X.

5. PARTICLE TRANSPORT

Radial particle transport comes from the correlated effects of density fluctuations and radial velocity fluctuations caused by $\tilde{E}_p$. This correlation can be calculated with frequency resolution from the Fourier transforms of $\tilde{n}(t)$ and $\tilde{v}_r(t) = \tilde{E}_p(t)/B_T$ [13–15]:

$$F(\omega) = C_{nE}(\omega)\, \tilde{n}(\omega)\, \tilde{v}_r(\omega)\cos\theta(\omega) \qquad (2)$$

where $F(\omega)$ is the frequency-dependent particle flux, $C_{nE}(\omega)$ is the coherence between $\tilde{n}$ and $\tilde{E}_p$ in a small frequency band around ω, and $\theta(\omega)$ is the frequency-dependent phase between $\tilde{n}$ and $\tilde{E}_p$: alternatively, the total flux can also be calculated without frequency resolution from the raw data:

$$F = \langle \tilde{n}\tilde{v}_r \rangle = C_{nE}(0)\langle \tilde{n} \rangle \langle \tilde{v}_r \rangle \qquad (3)$$

where $C_{nE}(0)$ is the zero-time correlation coefficient between $\tilde{n}$ and $\tilde{E}_p$, and $\langle \tilde{n} \rangle$ and $\langle \tilde{v}_r \rangle$ are the total root-mean-square fluctuation levels. Note that this process gives only the fluctuation-induced transport, so does not include steady diffusive or convective flows, and that it assumes $\tilde{T}_e \ll \tilde{\phi}$ in order to interpret the measured floating potential as the space potential [16].

Radial particle fluxes were calculated using data from both 1-D and 2-D probe arrays according to Eqs (2) and (3) (only three adjacent probes were used to measure $\tilde{n}$ and $\tilde{E}_p$ locally). The results were very similar to those obtained previously at Caltech [13], Pretext [14], Text [15], and TV-1 [17] using a similar technique; namely, that the calculated fluxes $F(\omega)$ were large and outward (corresponding to $\theta(\omega) \approx 0°$) over the radial range of $r/a \approx 0.85-0.95$, although the coherence between $\tilde{n}$ and $\tilde{E}_p$ was typically a rather low $C_{nE}(\omega) \approx 0.2$ 0.5 (i.e. not all of the $\tilde{n}$ amplitude was contributing to the outward particle flux). Using the local flux measurement made in the centre of the 2-D array, one can also derive an effective particle diffusion coefficient in order to compare these fluxes to theoretical predictions (Section 6.4).

6. DISCUSSION

6.1. General remarks

In this paper the spatial structure of tokamak turbulence was described in some detail. Our general conclusion is that this structure is best described as 'turbulent' in the sense that the local correlation

lengths are short compared to the size of the discharge, that both the frequency and wavenumber spectra of the $\tilde{n}$ are very broad, and that no obviously coherent structure was ever present in this set of data (see, for example, Figs 3, 5, 10 and 11). In this sense, the existence of turbulent transport associated with this $\tilde{n}$ and $\tilde{\phi}$ is not surprising, especially considering the large relative fluctuation levels measured in this edge region (Fig.6).

Measurements of local density and potential fluctuations made using these probe techniques are at present the only means by which the anomalous transport effects of tokamak density turbulence can be directly assessed. Although the calculated radial particle flux rates due to this turbulence are at least qualitatively in agreement with expected edge particle loss rates (see Sections 5 and 6.5 below), it is not possible at present to make any inferences concerning possible relations between edge turbulence and global particle or energy transport. This is simply because the turbulence levels and associated transport effects are strong functions of radius, such that these measurements at $r/a \approx 0.85-1.0$ cannot be extrapolated to the confinement region at $r/a \approx 0.5$.

However, these edge measurements are of direct relevance to questions concerning cross-field particle and/or impurity transport in the limiter or divertor regions at the edges of large tokamaks, where the plasma parameters may be similar to those in the present experiment [9]. For example, large cross-field particle transport rates such as suggested by the turbulence measurements of Section 5 can have a beneficial effect by increasing the scrape-off layer thickness behind a limiter's leading edge, thus allowing a more diffuse heat loading and a greater particle pumping than would be the case for classical cross-field transport.

Since edge turbulence such as described here is present for all normal operating regimes of the tokamak [1], the practical design of limiters and/or divertors will eventually be improved through better knowledge of the diffusive effects of edge turbulence. It is also possible that some subtle interaction occurs between the edge plasma and the central confinement region, such that improved global plasma confinement might be obtained through direct or inadvertent modification of the edge turbulence.

In the following Sections 6.2 to 6.5 the experimental results of Sections 3 to 5 are compared to recent theoretical models for edge turbulence. The relationship between these results and other recent experimental work on edge turbulence will be discussed in Section 6.6.

6.2. Spatial structure

The main experimental results on spatial structure are the comparisons between average poloidal and radial correlation lengths in Fig.10, the poloidal and 2-D k-spectra in Figs 5 and 11, and the examples of the instantaneous spatial structure in Figs 7 and 8. Taken together, these results suggest a strongly turbulent edge plasma state, i.e. one in which little trace of any linear instability remains and in which the fluctuations significantly perturb the background equilibrium.

The instantaneous 2-D patterns of $\tilde{n}$ and $\tilde{\phi}_f$ shown in the contour plots of Fig.8 look remarkably similar to 2-D contour plots calculated numerically from recent non-linear collisional drift-wave models [2, 3] (the edge plasma is marginally collisional [1]). These models predict broad k-spectra with a maximum amplitude at typically $k_p r_s \cong 0.3$ and broad frequency spectra at fixed k similar to Fig.5(a). Closer agreement with the observed peak of the $\tilde{n}(k_p)$ spectrum at $k_p r_s \cong 0.1$ is found by a recent non-linear analytic theory [4].

Although these non-linear collisional drift wave models are sufficient to reproduce the complexity in the experimental results, it is not yet clear that the underlying instability is necessarily a drift wave. Non-linear models based on rippling modes also reproduce several features of this turbulent structure, such as the relatively small poloidal wavenumber and the poloidal/radial $\tilde{n}$ and $\tilde{\phi}$ asymmetry [6], and the magnetic fluctuation correlation lengths [5].

The toroidal structure of this turbulence was not investigated in this paper; however, previous probe measurements on Macrotor [18] and Pretext [14] have shown that the toroidal correlation lengths are much longer than the radial or poloidal correlation lengths (similar conclusions were reached in scattering measurements [7, 8]). Thus the 3-D structure of the $\tilde{n}$ perturbations most likely consists of toroidally elongated 'filaments' qualitatively similar to those seen in visible-light emission from the ASDEX edge plasma [19, 20].

6.3. Propagation velocity

The poloidal propagation velocities in the edge region are mainly in the ion diamagnetic drift direction, as is shown in Figs 4 and 12. The phase velocities as measured by the $\tilde{n}(\omega, k_p)$ spectra are also predominantly in the ion direction, as is shown in Fig.5(a). This contrasts with the drift wave model predictions of electron direction propagation at about the electron

diamagnetic drift speed v_*, which for the profiles of Fig.6 should be $v_* = (1.5-2.0) \times 10^5 \text{cm} \cdot \text{s}^{-1}$ approximately independent of radial position.

However, the outward radial electric field of $\langle E_r \rangle = 15 \text{ V} \cdot \text{cm}^{-1}$ implied by the space potential profile of Fig.6(b) is more than large enough to reverse the apparent direction of propagation in the lab frame due to the E_r/B_T drift. This drift speed is about $6 \times 10^5 \text{cm} \cdot \text{s}^{-1}$ in the ion direction, approximately independent of the radial position, implying that the net phase speed should be about $4 \times 10^5 \text{cm} \cdot \text{s}^{-1}$ in the ion direction. The measured 'group' speed from the delayed-time correlation functions is typically $7 \times 10^5 \text{cm} \cdot \text{s}^{-1}$ (Fig.12), i.e. somewhat larger than this expectation (although not outside the combined uncertainties involved in estimating the local gradients).

The origin of the radial electric field in the edge may be related to the local ambipolarity condition for particle flow into a limiter since the local $\phi_s \approx 3T_e$ (see Fig.6). Thus the ion direction propagation may be confined to regions in contact with the limiter (in which the electron temperature, and hence the space potential, is also a decreasing function of radius).

6.4. Fluctuation levels

The large relative fluctuation levels $\tilde{n}/n \cong 0.2-0.5$ shown in Fig.6 are consistent with previous experimental results on edge turbulence (see Section 6.6), and also with the qualitative expectation that the strong gradients found near the plasma boundary can provide a mechanism for the growth of large fluctuations. The simple quantitative argument that the local fluctuations grow until they cancel out the density gradient leads to the 'mixing-length' scaling $\tilde{n}/n = (k_r L_n)^{-1}$ [3]. Here we have $k_r \cong 1/L_r$ so that $\tilde{n}/n = L_r/L_n = 0.7/5 \approx 15\%$, i.e. the observed fluctuation level is at least approximately given by the mixing-length formula (actually, the local fluctuations can 'overshoot' this level and for short times invert the local density gradient, as shown in Fig.7).

The results from non-linear collisional drift wave models are generally $\tilde{n}/n = (2-5) r_s/L_n$, where r_s is the ion gyroradius (evaluated at $T_i = T_e$) and L_n is the density gradient scale length [3, 4]. For the present parameters and profiles (Fig.6), we find $r_s/L_n = 3-4\%$ all across the array, so that for this experiment $\tilde{n}/n = (5-10) r_s/L_n$ (the constant of proportionality is about twice that found previously [1], since for this 2-D probe array L_n is larger than, T_e is smaller than, but $\tilde{n}/n$ is similar to, the previous results). In another drift-wave model [2] $\tilde{n}/n = \sqrt{r_s/L_n} \approx 20\%$ for the

180

present parameters. Rippling mode models can also reproduce density fluctuation levels up to 25% [6].

The fluctuations in $\tilde{\phi}_f$ might provide a clue to the mechanism of the instability. From Fig.6 it appears that $e\tilde{\phi}_f/T_e \approx \tilde{n}/n \approx 0.5$ at 0.5 cm into the plasma, but that $e\tilde{\phi}_f/T_e > \tilde{n}/n$ farther in towards the plasma centre. These profiles were checked by using a single movable probe in a limiterless discharge, and approximately the same results were obtained, i.e. $e\tilde{\phi}_f/T_e \approx \tilde{n}/n \approx 0.4$ at 1.5 cm into the plasma, $e\tilde{\phi}_f/T_e > \tilde{n}/n$ farther into the plasma, but with a clear decrease of $e\tilde{\phi}_f/T_e$ to zero very near the wall where $\tilde{n}/n > 0.5$. Similar results were first reported in Pretext [12].

The decrease of $e\tilde{\phi}_f/T_e$ near the wall may be due to the non-linear Boltzmann relation $(\tilde{n}+n)/n = \exp(e\tilde{\phi}/T_e)$; however, the relative increase in $e\tilde{\phi}/T_e$ farther into the plasma is more difficult to explain; perhaps this indicates the presence of small-scale convective cells or rippling modes [6] which can have $e\tilde{\phi}/T_e > \tilde{n}/n$. It should be noted that the $e\tilde{\phi}/T_e$ estimates are much more uncertain than those of $\tilde{n}/n$, because of the need to measure T_e separately and because of the possible influence of temperature fluctuations on $\tilde{\phi}_f$ [16].

6.5. Particle diffusion

For the case of the 2-D probe array, the net fluctuation-induced particle flux F calculated from Eq.(3) can be converted into a local particle diffusion coefficient using:

$$F = D \, dn/dx \tag{4}$$

where dn/dx is the density gradient at the probe used to measure F (i.e. 1.5 cm from the wall). Combining Eq.(4) with Eq.(3) to eliminate the dependence on the absolute value of the local n, we have:

$$D = C_{nE}(0) \langle \tilde{n}/n \rangle \langle \tilde{v}_r \rangle L_n \tag{5}$$

where $C_{nE}(0)$ is the zero-time correlation coefficient between the $\tilde{n}$ and $\tilde{E}_p$ signals, $\langle \tilde{v}_r \rangle$ is the local root-mean-square fluctuation level in the fluid velocity, and L_n is the local density gradient scale length. For the measurements made near the centre of the 2-D array $C_{nE}(0) \cong 0.2$, $\tilde{n}/n = 0.22$, $\langle \tilde{v}_r \rangle = 5 \times 10^5 \, \text{cm} \cdot \text{s}^{-1}$, and $L_n = 5$ cm, thus $D = 10^5 \, \text{cm}^2 \cdot \text{s}^{-1}$. This is about twice the value calculated from the Bohm formula, $D = 6.25 \, T_e(\text{eV})/B_T(\text{G})$.

An interesting check of this result comes from a calculation of the D needed to produce the observed 'scrape-off layer' behind the leading edge of the 2-D probe support structure itself. Assuming as

usual [9] that the particles found behind the limiter arrive there by cross-field diffusion, and that the residence time of an ion in the scrape-off region is approximately $q\pi R/c_s$ (where q is the safety factor at the wall, R the major radius, and c_s the ion sound speed), we have:

$$D = L_n^2 c_s/(q\pi R) \tag{6}$$

or $D \cong 2 \times 10^5 \, \text{cm}^2 \cdot \text{s}^{-1}$. Of course, this estimate of D is uncertain to at least a factor of two; nevertheless, there appears to be a qualitative agreement between this result and the one derived from the fluctuation measurements.

Collisional drift wave models predict several different forms for D depending on the details of the theory. Waltz [3] compares his numerical results to a mixing-length rule such that $d = 0.8\gamma/k_r^2$, where γ is the maximum linear driving rate. If we approximate γ by the inverse of the measured auto-correlation time t_A, we find $D = 10^5 \, \text{cm}^2 \cdot \text{s}^{-1}$ for the measured $t_A = 10^{-5}$ s and $k_r = 1 \, \text{cm}^{-1}$. The numerical results of Wakatani and Hasegawa [2] were fit by $D = 0.2 T_e/eB_T$ (i.e. the Bohm formula with a factor of 0.2 instead of 1/16), hence $D = 1.5 \times 10^5 \, \text{cm}^2 \cdot \text{s}^{-1}$ here. The analytic theory of Terry and Diamond [4] presents a formula for D which has the approximate magnitude of Bohm diffusion but with a scaling $D = n^{2/3}$, which seems to agree qualitatively with the increase in particle flux farther into the plasma seen here and in the Texas tokamaks. Rippling modes can also produce large particle diffusion [6]. Thus we can conclude (at least tentatively) that the large outward particle flux inferred from the turbulence measurements is responsible for the observed cross-field particle diffusion into the scrape-off region, and that this process is comprehensible in terms of non-linear edge instability theory.

6.6. Relation to other experimental results

The structure of $\tilde{n}$ described here is roughly consistent with several electromagnetic scattering measurements of edge turbulence [7, 8], which have previously shown approximately isotropic $\tilde{n}(k_r, k_p)$ spectra with wavenumbers in the same range $(1-10 \, \text{cm}^{-1})$ and broad frequency spectra at fixed k similar to Fig.5(a). These results are also consistent with recent two-probe measurements on Text [14] and Pretext [15], which have shown broad $\tilde{n}(k_p)$ spectra similar to Fig.5 and an approximately 2/1 asymmetry in the radial-versus-poloidal structure somewhat similar to Fig.10. Previous

two-probe correlation measurements on Macrotor [18] showed an asymmetry of about 5/1 in poloidal/radial correlation lengths of $\tilde{\phi}_f$, compared to the ratio 2.5/1 shown in Fig.10.

Probe measurements in Pretext [14] and Text [15] also showed ion direction propagation in the edge, and in Text this propagation was seen to reverse to the electron direction nearer to the plasma centre, similarly to Figs 4 and 12 here. In Text, this ion-direction propagation was quantitatively explained by the measured outward radial electric field $\langle E_r \rangle \cong 30$ V·cm⁻¹ in the limiter shadow region, and the probe-measured propagation speed also matched the FIR laser measured speed where these two measurements overlapped [21]. Recent measurements on the TM-4 tokamak have also shown positive space potentials in the edge region along with ion-diamagnetic particle flow [22].

The relative density fluctuation levels $\tilde{n}/n = 20-50\%$ (Fig.6) are in the range of previous probe and scattering measurements in the tokamak edge region [7, 8]; for example, in Text both the probe- and the FIR-laser-scattering-inferred fluctuation levels were about $\tilde{n}/n > 15\%$ near the outer limiter [21]. Potential fluctuations with spectra and correlation lengths similar to $\tilde{n}$ have also been reported previously with $e\tilde{\phi}/T_e \gtrsim \tilde{n}/n$ [14, 15].

The results on $\tilde{E}_p \times B$-induced particle transport described in Section 5 are at least qualitatively similar to a preliminary result obtained on this machine using a movable triple probe [13], and to similar movable probe measurements on Pretext [14], Text [15], and TV-1 [17]. In each case the phase angle between $\tilde{n}$ and $\tilde{E}_p$ was roughly zero degrees for the low-frequency, high-amplitude part of the spectrum below about 200 kHz, implying a large outward flux of particles even though the correlation coefficient between $\tilde{n}$ and $\tilde{E}_p$ was substantially less than 1.0.

7. SUMMARY

The spatial structure of tokamak edge turbulence was measured by using compact Langmuir probe arrays. Results included the following:

1) The extended 32-probe 1-D poloidal array showed broad $\tilde{n}(\omega, k_p)$ spectra with an average poloidal correlation length $L_p = 1.0-1.5$ cm and a peak in the $\tilde{n}(k_p)$ spectrum at $k_p r_s \approx 0.1$.

2) The smaller 2-D radial-versus-poloidal array also showed broad $\tilde{n}(k_p, k_r)$ spectra with $L_p = 1.1$ cm but with $L_r = 0.7$ cm.

3) The 2-D structure of the floating potential fluctuations $\tilde{\phi}_f$ was qualitatively similar to the $\tilde{n}$, with $L_p = 1.2$ cm and $L_r = 0.5$ cm.

4) The unaveraged 2-D structure actually consists of localized 'blobs' of relatively higher or lower $\tilde{n}$ $\tilde{\phi}$, which move irregularly both radially and poloidally through the edge region [12].

5) The poloidal propagation velocity was predominantly in the ion diamagnetic drift direction, most likely because of the local outward radial electric field.

6) Fluctuation levels were typically $e\tilde{\phi}_f/T_e \approx \tilde{n}/n \approx 0.5$ at $r/a = 0.95$.

7) Fluctuation-induced radial particle transport was calculated to be outward and comparable to the Bohm-level diffusion usually found in the edge or scrape-off region.

This strong turbulence in the tokamak edge region is most likely associated with the relatively large gradients maintained near the plasma boundary. Modification of these gradients can significantly change the edge stability; for example, it was recently shown in the divertor tokamak PDX [23] that quasi-coherent bursts of edge $\tilde{n}$ can appear in H-mode plasmas. It remains to be seen whether this edge turbulence has some connection with the overall particle and/or heat confinement properties of the tokamak.

ACKNOWLEDGEMENTS

REFERENCES

[1] ZWEBEN, S.J., GOULD, R.W., Nucl. Fusion 23 (1983) 1625.

[2] WAKATANI, M., HASEGAWA, A., Phys. Fluids 27 (1984) 691.

[3] WALTZ, R., Phys. Fluids 28 (1985) 577.

[4] TERRY, P.W., DIAMOND, P.H., Theory of Dissipative Density Gradient Driven Turbulence in the Tokamak Edge, Univ. Texas Rep. IFSR No.114 (1984).

[5] CARRERAS, B.A., GAFFNEY, P.W., HICKS, H.R., CALLEN, J.D., Phys. Fluids 25 (1982) 1231.

[6] GARCIA, L., DIAMOND, P.H., CARRERAS, B.A., CALLEN, J.D., Theory of Resistivity Gradient Driven Turbulence, Univ. Texas Rep. No.146 (1984).

[7] LIEWER, P.C., Measurements of microturbulence in tokamaks and comparisons with theories of turbulence and anomalous transport, to be published by Nucl.Fusion.

[8] SURKO, C.M., SLUSHER, R.E., Science 221 (1983) 4613.

[9] ZWEBEN, S.J., TAYLOR, R.J., Nucl. Fusion 23 (1983) 513.

[10] COSSO, F., ZWEBEN, S., Analog delay line based multi-channel digitizer, to be published in Rev. Sci. Instrum. 56 (1985).

[11] ZWEBEN, S.J., LIEWER, P.C., GOULD, R.W., Phys. Fluids 27 (1984) 691.

[12] ZWEBEN, S.J., GOULD, R.W., Phys. Fluids 28 (1985) 974.

[13] ZWEBEN, S.J., LIEWER, P.C., GOULD, R.W., J. Nucl. Mater. 111/112 (1982) 39 (Proc. 5th Int. Conf. Plasma-Surface Interactions, Gatlinberg, Tennessee, USA).

[14] LEVINSON, S.J., BEALL, J.M., POWERS, E.J., BENGTSON, R.D., Nucl. Fusion 24 (1984) 527.

[15] RITZ, Ch.P., BENGTSON, R.D., LEVINSON, S.J., POWERS, E.J., Phys. Fluids 27 (1984) 2956.

[16] McCHESNEY, J., ZWEBEN, S.J., GOULD, R.W., Edge temperature fluctuations in the Caltech tokamak, submitted to IEEE Trans. Plasma Sci.

[17] IVANOV, R.S., private communication (1984).

[18] ZWEBEN, S.J., TAYLOR, R.J., Nucl. Fusion 21 (1981) 193.

[19] GOODALL, D.H.J., J. Nucl. Mater. 111/112 (1982) 11.

[20] ZWEBEN, S.J., McCHESNEY, J., GOULD, R.W., Nucl. Fusion 23 (1983) 825.

[21] BROWER, D.L., BENGTSON, R.D., GENTLE, K.W., KOCHANSKI, T.P., LEVINSON, S.J., et al., in Plasma Physics and Controlled Nuclear Fusion Research (Proc. 10th Int. Conf. London, 1984), Vol.1, IAEA, Vienna (1984) 273.

[22] BUGARYA, V.I., GORSHKOV, A.V., GRASHIN, S.A., IVANOV, I.V., et al., Sov. Phys — JETP Lett. 38 (1983) 404.

[23] SLUSHER, R.E., SURKO, C.M., VALLEY, J.F., CROWLEY, T., MAZZUCATO, E., McGUIRE, K., Phys. Rev. Lett. 53 (1984) 667.